Published in final edited form as:
Nat Chem. 2021 October 01; 13(10): 977–981. doi:10.1038/s41557-021-00753-8.

Atomistic Dynamics of Elimination and Nucleophilic Substitution Disentangled for the $F^- + CH_3CH_2Cl$ Reaction

Jennifer Meyer[#1,†], **Viktor Tajti**[#2], **Eduardo Carrascosa**[#1,§], **Tibor Győri**[2], **Martin Stei**[1,$], **Tim Michaelsen**[1], **Björn Bastian**[1,$$], **Gábor Czakó**[2,‡], **Roland Wester**[1,¶]

[1]Institut für Ionenphysik und Angewandte Physik, Univerisität Innsbruck Technikerstraße 25, 6020 Innsbruck, Austria

[2]MTA-SZTE Lendület Computational Reaction Dynamics Research Group, Interdisciplinary Excellence Centre and Department of Physical Chemistry and Materials Science, University of Szeged, Rerrich Béla tér 1, Szeged H-6720, Hungary

[#] These authors contributed equally to this work.

Abstract

Chemical reaction dynamics are studied to follow and understand the concerted motion of several atoms while they rearrange from reactants to products. With the number of atoms growing, the number of pathways, transition states, and product channels also increases and rapidly presents a challenge to experiment and theory. Here, we disentangle the competition between bimolecular nucleophilic substitution (S_N2) and base-induced elimination (E2) in the polyatomic reaction F^- + CH_3 CH_2 Cl. We find quantitative agreement for the energy- and angle-differential reactive scattering cross sections between ion imaging experiments and quasi-classical trajectory simulations on a 21-dimensional potential energy hypersurface. The anti-E2 pathway is most important, but the S_N2 pathway becomes more relevant as the collision energy is increased. In both cases the reaction is dominated by direct dynamics. Our study presents atomic level dynamics of a major benchmark reaction in physical organic chemistry, thereby pushing the number of atoms for detailed reaction dynamics studies to a size that allows applications in many areas of complex chemical networks and environments.

[‡] gczako@chem.u-szeged.hu . [¶] roland.wester@uibk.ac.at .
[†]present address: Fachbereich Chemie, Technische Universität Kaiserslautern, Erwin-Schrödinger Str. 52, 67663 Kaiserslautern, Germany
[§]present address: Laboratoire de Chimie Physique Moléculaire, École Polythechnique Fédérale de Lausanne, EPFL SB ISIC LCPM, Station 6, CH-1015 Lausanne, Switzerland
[$]present address: Swarovski Technology, D. Swarovski KG, Swarovskistraße 30, 6112 Wattens, Austria
[$$]present address: Department of Physics and Astronomy, Aarhus University, Ny Munkegarde 120, 8000 Aarhus C, Denmark

Author contributions

Authors contributions: E.C., J.M., and M.S. carried out the experiment. J.M. and E.C. analyzed the data. B.B. extended the data analysis program suite. T.M. and B.B. contributed to data discussion and interpretation. V.T. and T.G. developed the potential energy surface. V.T. performed the trajectory simulations and analyzed the data. G.C. and R.W. supervised the project. J.M. and R.W. prepared the manuscript, V.T. and G.C. contributed the theoretical sections.

Competing Interests

The authors have no competing interests to declare.

Europe PMC Funders Author Manuscripts

Chemical reactions of small molecules can today be understood with an impressive level of detail [1–3]. However, once more than four atoms are involved in a chemical reaction, the atomistic dynamics of bond cleavage and bond formation become challenging to experiment and theory, as the number of involved vibrational modes, reaction pathways, transition states, and product channels increases rapidly [4, 5]. The fundamental process to clarify is the motion and rearrangement of all involved atoms during a reaction for all posssible pathways[5–12]. A ubiquitous example is the competition of bimolecular nucleophilic substitution (S_N2) versus base-induced elimination (E2). Both reactions are part of numerous synthesis protocols in organic chemistry due to their stereo-specificity. The dynamics of these reactions therefore constitute ma jor benchmark systems in physical organic chemistry[13–18]. Separating S_N2 and E2 reactions is complicated by the fact that several important aspects affect both reactions similarly: the attacking nucleophile/base, the type of leaving group, and the polarity of the solvent. Only the steric environment at the reaction center allows to directly manipulate the branching ratio. Studies under single-collision conditions, which allow focusing on the intrinsic dynamics while excluding solvation effects, are complicated by the fact that both reactions usually form the same product ion and can not be distinguished by standard mass spectrometry. Several elaborate methods have therefore been employed to distinguish between the two reactions in the gas phase[13, 14, 17,19]. Interestingly, S_N2 leads to the thermodynamically more stable product while E2 features the lower transition state barrier, i. e. E2 forms the kinetically preferred product. S_N2 and E2 reaction coordinates in the gas phase commonly follow a double-well path with submerged barriers accompanied by entrance and exit channel complexes[18, 20] as opposed to a single barrier in solution. Energy partitioning for gas-phase S_N2 reactions was found to often occur non-statistically[21]. In certain cases the reaction may even proceed by avoiding its minimum energy structures altogether[22].

A model reactant that allows for both elimination (Reaction 1) and nucleophilic substitution (Reaction 2) is CH_3CH_2Cl with its primary carbon center (exothermicities are taken from Refs. [15] and [23]). The ethyl residue is not as sterically congested at the α-carbon as to fully suppress the S_N2 reaction (Fig. 1a):

$$F^- + CH_3CH_2Cl \rightarrow Cl^- + HF + CH_2CH_2 \qquad \Delta_R H(E2) = -0.96\text{eV} \tag{1}$$

$$\rightarrow Cl^- + CH_3CH_2F \qquad \Delta_R H(S_N2) = -1.44\text{eV} \tag{2}$$

S_N2 reactions in the gas phase are known to have rich and complex atomistic dynamics[24]. Recently, we could identify fingerprints for atomistic dynamics of E2 reactions as well, using measurements of their differential scattering cross sections[17, 25]. Trajectory simulations for elimination have so far been limited to on-the-fly dynamics[16, 26] with statistics not sufficient for a direct comparison with the experiment. The reaction coordinates for the three most important pathways, S_N2, anti-E2, and syn-E2, feature submerged barriers with anti-E2 having the least congested transition state (Fig. 1a)[15, 23]. S_N2 and anti-E2 are connected by a shared ion-dipole-bound pre-reaction minimum[15, 27], whereas in syn-E2 a hydrogen-bonded complex is found[15].

Using only stationary properties can be misleading to predict atomistic mechanisms, direct versus indirect dynamics, and energy partitioning [28]. To investigate S_N2 and E2 reactions at this level of detail, experiments and theory need to directly probe the atomic-level dynamics. In case of elimination, tracing the internal excitation of the molecular products can be obscured by the three-body break-up (Fig. 1b). For experiments under single collision conditions that probe one ionic product, only the combined internal excitation of both molecular products, together with their translational recoil, can be extracted. Tra jectory simulations with sufficiently high statistics can be used to disentangle the three contributions.

Results

We use experimental differential cross sections from ion-molecule crossed beam 3D velocity map imaging (VMI) experiments and quasi-classical trajectory (QCT) simulations on a new full-dimensional (21 D) potential energy surface to study the $F^- + CH_3CH_2$ Cl reaction. The combination of both methods allows the kinematically complete characterization of the S_N2 and E2 reactions as well as their competition. Experimental angle and energy differential cross sections for Cl^- product ions are presented in Fig. 2a–e. The Cl^- velocity distributions are shown in the center-of-mass frame for five relative collision energies E rel in the range from 0.35 to 1.96 eV. At the lowest collision energy a clear forward-backward symmetry is visible together with widespread isotropic scattering and isotropic scattering into low product ion velocities around the center-of-mass (Fig. 2a). This scattering feature is typical for indirect S_N2 reactions[29]. The forward-backward symmetric events are due to a large impact parameter indirect complex-mediated mechanism that was recently identified in another E2 reaction[25]. With increasing collision energy the forward-backward symmetry is lifted. The images become dominantly isotropic with some scattering into the forward hemisphere ($\theta = 0° – 90°$) at small angles (Fig. 2b–e). The integral angular distributions (Fig. 2f-j, black) confirm the trend towards forward scattering with some minor backward scattering appearing at the two highest collision energies (Fig. 2i,j). Forward reactive scattering is a fingerprint of direct E2 dynamics[17,25]. Backward scattering is a signature of the direct rebound (DR) mechanism known for S_N2[28, 29]. Cuts in velocity space confirm the presence of the direct rebound by the characteristic umbrella of events in the backward hemisphere at high Cl^- velocities (Supplementary Fig. 2). Integral angular distributions from the QCT simulations (Fig. 2f-j, green) quantitatively reproduce the experiment at all five collision energies. The remaining differences are well accounted for by the statistical and systematic uncertainties of both simulation and experiment. The simulations capture the forward-backward symmetry and isotropic contribution at the lowest collision energy and the shift toward forward scattering at higher collision energies. The experimental and simulated product ion kinetic energy distributions (Fig. 2k-o; exp: black, sim: green) also show very good agreement. The distributions reveal a broadening with increasing collision energy, while the maxima do not markedly shift. This decoupling of product ion kinetic energy from reactant collision energy has been identified as a signature for indirect dynamics in case of pure E2 reactions[25].

Discussion

The excellent agreement between experiment and simulations allows us to disentangle the competition between S_N2 and E2, plotted in orange and red in Fig. 2f–o. At 0.35 eV both reactions scatter into all angles (Fig. 2f), but with different dynamic signatures: E2 leads to forward-backward symmetric scattering and S_N2 to almost isotropic scattering. This follows patterns known from S_N2 reactions of CH_3Cl and E2 reactions of $(CH_3)_3CCl$ with F^- [25, 28] and is ascribed to complex-mediated indirect dynamics. With increasing collision energy, simulations reveal more anisotropic angular distributions (Fig. 2h–j), which is attributed to a growing contribution of direct scattering. Whereas scattering into the forward hemisphere is almost pure elimination at all collision energies (> 80 %), S_N2 contributes up to half of the events scattered into the backward hemisphere at the two highest collision energies. This superposition causes the seemingly wholly isotropic indirect character of the experimental velocity images. The prevalence of E2 over S_N2 dynamics is also seen in the much larger range of attack angles that lead to the elimination pathway (Supplementary Fig. 5).

To test the contribution of direct reaction dynamics to the overall scattering, the fraction of simulated tra jectories that swiftly form products without forming a transient intermediate complex is determined. This confirms that E2 and S_N2 shift from highly indirect to direct character with increasing collision energy (Fig. 3a). Comparable direct fractions have been found for the pure S_N2 reaction of $F^- + CH_3Cl$ [28]. In contrast, E2 reactions with the bulkier reactant $(CH_3)_3CCl$ are much more indirect [25]. Reactions of ethyl halides with different bases and leaving groups show similar direct fractions[16, 17,26,30].

Besides the Cl^- product ion, also $FH...Cl^-$ and trace amounts of CH_3CHCl^- are found in both experiment and simulation, following Reaction 3 and 4.

$$F^- + CH_3CH_2Cl \rightarrow FH\cdots Cl^- + CH_2CH_2 \qquad \Delta_R H\left(FH\cdots Cl^-\right) = -1.93\text{eV} \tag{3}$$

$$\rightarrow CH_3CHCl^- + HF \qquad \Delta_R H(PT) = 1.15\text{eV} \tag{4}$$

Experimental product branching ratios, which are extracted by time-of-flight traces (Supplementary Fig. 3), compare well with the relative integral cross sections for the two major product ions (Supplementary Table 3), as shown in Fig. 3b. The simulated $FH...Cl^-$ fraction lies somewhat above the experimental fraction, which may indicate late dissociation of this product that is not captured within the time frame of the QCT simulations. CH_3CHCl^- is formed in an endothermic proton transfer (PT), Reaction4. It is most likely a transient species that can undergo 1,2-H-shift and subsequently form elimination products. Similar branching ratios for the three product ion species have been found for $F^- + CH_3CH_2I$[17].

Figure 3b also shows the relative contributions for the S_N2, anti-E2, and syn-E2 reaction pathways that have been extracted from the QCT results (see Methods section for details). Anti-E2 is by far the dominant reaction at all collision energies. While its contribution drops with increasing collision energy, that of syn-E2 rises. S_N2 becomes more important at higher collision energies accounting for 30 % of the total reactivity at 1.96 eV. The reason for this

behavior is found in the reaction probability as a function of impact parameter (Supplementary Fig. 4). In case of anti-E2, these probability functions retain a significant contribution of large reactive impact parameters, which remains even at the highest collision energy, where at small impact parameters the S_N2 reaction has a higher probability. Anti-E2 and syn-E2 give comparable angular distributions (Supplementary Fig. 7). Only at the lowest collision energy, the forward-backward peaked signature of anti-E2 is not present for syn-E2. The syn-E2 reaction branches into two product ion channels: Cl^- (Reaction1) and $FH...Cl^-$ (Reaction3). Both channels are formed with a comparable probability at low collisions energies, whereas Cl^- formation dominates at high collision energies (Fig. 3b). This is likely a consequence of an increased dissociation probability of $FH...Cl^-$ into HF and Cl^-, which requires approx. 1eV energy (Fig.1a). Experimental scattering images and QCT results for $FH...Cl^-$ product ions show mostly forward scattering (Supplementary Fig. 8).

Due to the three-body break-up in E2, the experiment cannot directly extract the amount of energy partitioned into internal excitation. Instead, the experimental data reveals the sum of the ro-vibrational excitation Eint of HF and C_2H_4 and the relative kinetic energy Erecoil from the recoil between the two neutral products (black line in Fig. 4). The trajectory simulations for the E2 reaction (red line in Fig. 4), however, allow one to separate the energy partitioning between HF and C_2H_4 internal excitation and their relative recoil energy. The QCT result deviates slightly from the experimental distribution, because the contribution from S_N2 reactions, which is part of the experimental data, has been filtered out. The total internal energy, the sum of HF and C_2H_4 internal excitation, is shown as gray shaded area in Fig. 4. It remains essentially constant with increasing collision energy. The full experimental or simulated distributions, however, which include the recoil energy (black and red traces), extend to larger energies. This is direct evidence that most of the additional collision energy is partitioned into recoil energy between the two neutral products. The dashed curves show the separate internal energy distributions for HF (blue) and C_2H_4 (green). HF is predominantly formed in its vibrational ground state, irrespective if it is formed by syn-E2 or anti-E2 (Supplementary Fig. 9). This is seen from the blue bars spaced by the vibrational quantum of the HF stretch. Hase and co-workers found a similar behavior for the proton transfer forming ICH_2^- and HF in reactions of $F^- + CH_3I$[31]. The internal excitation of C_2H_4 increases only slightly with collision energy, which is evident by a growing tail of the distribution. For the S_N2 reaction, the comparison between the simulated internal excitation distribution for the CH_3CH_2F product and the experimental data is shown in Supplementary Fig. 10. With the reaction becoming increasingly direct when the collision energy is increased, the internal excitation decreases slightly.

Conclusion

The present study investigates a benchmark reaction for complex polyatomic reaction dynamics in a combined approach of experiment and theory. We have probed the differential cross section to disentangle the energy dependent atomistic dynamics and competition of S_N2 versus E2 reactions. The reaction of $F^- + CH_3CH_2Cl$ is dominated by direct dynamics despite the numerous internal degrees of freedom, except at the lowest collision energy. The energy partitioning in the three-body break-up of E2 reactions is complex with a significant amount of energy channeled into the recoil of the two neutral products. It is remarkable that

the reaction dynamics of this complex reaction can be disentangled into distinct atomic-level mechanisms that have been identified through their fingerprints on the differential cross sections in systems that undergo either pure S_N2 or only E2 reactions. This clearly supports the notion of a bottom up approach to understand multidimensional reaction dynamics on its way to real-life chemical reactions. Furthermore, with the intrinsic reactivity and dynamics on the ground state potential energy surface fully characterized, it becomes possible to track down the effects of manipulating such reactions, for example by functionalization, micro-hydration, or selective internal excitation of the reactants.

Methods

Experiment

Reactive crossed beam scattering in combination with 3D velocity map imaging[33] was used to record differential cross sections. The experimental setup and experimental procedure has been described before[34, 35]. In brief, ions are produced by a pulsed plasma discharge ignited in a supersonic beam (10% NF3 in Argon). F^- ions are extracted perpendicularly to the initial direction of the expansion by a Wiley-McLaren type electrode arrangement and loaded into an octupole radio frequency ion trap operated at room temperature. Ions are stored for 40 ms and collisions with N_2 buffer gas reduce the translational energy spread of the ion ensemble. Ions are ejected from the trap and guided into the interaction region of the velocity map imaging spectrometer. There, the ion beam is intersected by a skimmed molecular beam of CH_3CH_2Cl seeded at a couple of percent in Helium. Densities in the interaction volume are such that the experiment operates under single collision conditions.

Cl^- product ions are extracted perpendicular to the scattering plane and mapped onto a position and time sensitive detector consisting of a multichannel plate phosphor screen combination with a CCD-camera recording the position of impact. Simultaneously, the arrival time is recorded by a photomultiplier tube which detects the photon signal emitted by the phosphor screen. Cylindrical symmetry allows us to display the three-dimensional velocity distributions in a two-dimensional representation to better compare to sliced images.

The energy and angular spreads of both reactant beams are determined using 2D velocity mapping and fitting of the resulting distributions. The translational temperature of the neutral beam (CH_3CH_2Cl in He) intheco-movingframeis≈150–200Kwhichmeansthat internal rotation of the methyl groups along the C-C axis is frozen out.[36]. The energy spread of the relative collision energy for the presented crossed beam experiments is in the range of 20–50 meV (1σ). A graphical representation of the experimental resolution at the collision energy of 0.35 eV is shown in the Supplementary Fig. 1. The experimental uncertainty for the resulting product kinetic and internal energy distributions is determined by error propagation of the reactant beams[34] and ranges from 150–250 meV.

Theory

We developed the first full-dimensional (21 D) analytical ab initio potential energy surface (PES) for the $F^- + CH_3CH_2Cl$ reaction using the Robosurfer program system[37] to automate

the construction of the PES and the permutationally-invariant monomial symmetrization approach (MSA)[38] to fit the energy points. The initial dataset of 5,319 structures was obtained by randomly modifying the Cartesian coordinates of the previously-known[15] stationary-point geometries. The *ab initio* energies were computed by the density-fitted explicitly-correlated second-order Møller-Plesset perturbation method (DF-MP2-F12) with the aug-cc-pVDZ basis set. Then, Robosurfer iteratively developed the PES by (1) running quasiclassical trajectories at different collision energies and impact parameters, (2) selecting configurations along the trajectories that most likely improve the quality of the PES, (3) performing ab initio computations at the DF-MP2-F12/aug-cc-pVDZ level with MOLPRO[39] and (4) fitting the energy point by MSA. At the final stage of the PES development the energy points were recomputed with a higher, composite ab initio level of theory: CCSD(T)-F12b/aug-cc-pVDZ + MP2-F12/aug-cc-pVTZ – MP2-F12/aug-cc-pVDZ, employing the gold-standard explicitly-correlated CCSD(T)-F12b method to provide an accurate description of electron correlation while the basis-set effects beyond aug-cc-pVDZ were described with the computationally less-expensive MP2-F12 method. The final PES was fitted to 35,474 energy points by a weighted linear least-squares method using a 5^{th}-order polynomial expansion of Morse-like variables, $\exp(-r_{ij}/a)$, a = 3 bohr, of r_{ij} inter-atomic distances, resulting in 11,241 terms (coefficients).

The analytical PES developed in this study allows efficient and accurate reaction dynamics (QCT) simulations for the nine-atomic F^- + CH_3CH_2Cl system. Standard normal-mode sampling[40] is used to prepare the quasiclassical vibrational ground state of the CH_3CH_2Cl reactant molecule, thereby incorporating the quantum-mechanical zero-point energy effects into the classical simulations. The initial distance of the reactants was 25 bohr, their relative orientation was randomly sampled, and impact parameters were scanned from zero to their maximum value with a step size of 0.5 bohr. We computed 1,000 tra jectories at each impact parameter at each of the following collision energies: 0.35, 0.83, 1.15, 1.60, and 1.98 eV. Each trajectory was propagated until the largest inter-atomic separation became 1 bohr larger than the largest initial one. Cross sections were computed using an impact-parameter-weighted numerical integration of the reaction probabilities over impact parameters.

More details of the experimental and theoretical methods are given in the Supplementary Information.

Supplementary Material

Refer to Web version on PubMed Central for supplementary material.

Acknowledgments

R.W. thanks the Austrian Science Fund (FWF), project P25956-N20, for support of this work. G.C. thanks the National Research, Development and Innovation Office-NKFIH, K-125317, the Ministry of Human Capacities, Hungary grant 20391-3/2018/FEKUSTRAT, and the Momentum (Lendület) Program of the Hungarian Academy of Sciences forfinancial support. We acknowledge KIFü for awarding us access to computational resource based in Hungary at Debrecen. J.M. acknowledges support by a Hertha-Firnberg fellowship of the Austrian Science Fund (T962-N34). E.C. acknowledges support by the DOC-fellowship of the Austrian Academy of Science.

Data Availability Statement

The presented data are provided in the online material accompanying this article.

References

1. Xie Y, et al. Quantum interference in H + HD → H_2 + D between direct abstraction and roaming insertion pathway. Science. 2020; 368 :767–771. [PubMed: 32409475]
2. Zhang X, Li L, Chen J, Liu S, Zhang DH. Feshbach resonances in the F + H_2O→ HF + OH reactio. Nat Commun. 2020; 11 :223. [PubMed: 31932595]
3. Yang T, et al. Enhanced reactivity of fluorine with para-hydrogen in cold interstellar clouds by resonance-induced quantum tunnellin. Nat Chem. 2019; 11 :744–749. [PubMed: 31235895]
4. Pan H, Liu K, Caracciolo A, Casavecchia P. Crossed beam polyatomic reaction dynamics: recent advances and new insight. Chem, Soc Rev. 2017; 46 :7517–7547. [PubMed: 29168517]
5. Liu K. Vibrational control of bimolecular reactions with methane by mode, bond, and stereo selectivit. Annu Rev Phys Chem. 2016; 67 :91–111. [PubMed: 26980310]
6. Brouard M, Parker DH, van de Meerakker SYT. Taming molecular collisions using electric and magnetic field. Chem Soc Rev. 2014; 43 :7279–7294. [PubMed: 25115818]
7. Zhao ZQ, Zhang ZJ, Liu S, Zhang DH. Dynamical barrier and isotope effects in the simplest substitution reaction via Walden inversion mechanis. Nat Commun. 2017; 8 14506 [PubMed: 28224993]
8. Estillore AD, Visger LM, Suits AG. Imaging the dynamics of chlorine atom reactions with alkenes. J Chem Phys. 2010; 133 074306 [PubMed: 20726641]
9. Herman Z, Futrell JH. Dynamics of ion-molecule reactions from beam experiments: A historical surve. Int J Mass Spectrom. 2015; 377 :84–92.
10. Wang Y, et al. Mode-specific S_N2 reaction dynamics. J Phys Chem Lett. 2016; 7 :3322–3327. [PubMed: 27505286]
11. Carrascosa E, Meyer J, Wester R. Imaging the dynamics of ion-molecule reaction. Chem Soc Rev. 2017; 46 :7498–7516. [PubMed: 29136081]
12. Xie J, Hase WL. Rethinking the S_N2 reactio. Science. 2016; 352 :32–33. [PubMed: 27034358]
13. Gronert S. Gas phase studies of the competition between substitution and elimination reaction. Acc Chem Res. 2003; 36 :848–857. [PubMed: 14622032]
14. Villano SM, Kato S, Bierbaum VM. Deuterium kinetic isotope effects in gasphase S_N2 and E2 reactions: A comparison of experiment and theory. J Am Chem Soc. 2006; 128 :736–737. [PubMed: 16417360]
15. Tajti V, Czakó G. Benchmark ab initio characterization of the complex potential energy surface of the F^- + CH_3CH_2Cl reaction. J Phys Chem A. 2017; 121 :2847–2854. [PubMed: 28338332]
16. Yang L, et al. Competing E2 and S_N2 mechanisms for the F^- + CH_3CH_2I reaction. J Phys Chem A. 2017; 121 :1078–1085. [PubMed: 28094946]
17. Carrascosa E, et al. Imaging dynamic fingerprints of competing E2 and S_N2 reaction. Nat Commun. 2017; 8 :25. [PubMed: 28638140]
18. Hamlin TA, Swart M, Bickelhaupt FM. Nucleophilic substitution (S_N2): Dependence on nucleophile, leaving group, central atom, substituents, and solven. ChemPhysChem. 2018; 19 : 1315–1330. [PubMed: 29542853]
19. Eyet N, Melko JJ, Ard SG, Viggiano AA. Effect of higher order solvation and temperature on S_N2 and E2 reactivit. Int J Mass Spectrom. 2015; 378 :54–58.
20. Hase WL. Simulations of gas-phase chemical reactions: Applications to S_N2 nucleophilic substitutio. Science. 1994; 266 :998–1002. [PubMed: 17779941]
21. Viggiano AA, Morris RA, Paschkewitz JS, Paulson JF. Kinetics of the gasphase reactions of chloride anion, Cl^- with CH_3Br and CD3Br: experimental evidence for nonstatistical behavior? J Am Chem Soc. 1992; 114 :10477–10482.
22. Sun L, Song K, Hase WL. A S_N2 reaction that avoids its deep potential energy minimu. Science. 2002; 296 :875–878. [PubMed: 11988565]

23. Czakó G, et al. Benchmark ab initio and dynamical characterization of the stationary points of reactive atom + alkane and S_N2 potential energy surface. Phys Chem Chem Phys. 2020; 22 :4298–4312. [PubMed: 31840714]
24. Xie J, et al. Identification of atomic-level mechanisms for gas-phase $X^- + CH_3Y$ S_N2 reactions by combined experiments and simulation. Acc Chem Res. 2014; 47 :2960–2969. [PubMed: 25120237]
25. Meyer J, et al. Unexpected indirect dynamics in base-induced elimination. J Am Chem Soc. 2019; 141 :20300–20308. [PubMed: 31782654]
26. Liu X, Zhang J, Yang L, Hase WL. How a solvent molecule affects competing elimination and substitution dynamics. Insight into mechanism evolution with increased solvation. J Am Chem Soc. 2018; 140 :10995–11005. [PubMed: 29968466]
27. Mugnai M, Cardini G, Schettino V. Substitution and elimination reaction of F^- with C_2H_5Cl: An ab initio molecular dynamics study. J Phys Chem A. 2003; 107 :2540–2547.
28. Stei M, et al. Influence of the leaving group on the dynamics of a gas-phase S_N2 reactio. Nat Chem. 2016; 8 :151–156. [PubMed: 26791898]
29. Mikosch J, et al. Imaging nucleophilic substitution dynamic. Science. 2008; 319 :183–186. [PubMed: 18187650]
30. Carrascosa E, Meyer J, Michaelsen T, Stei M, Wester R. Conservation of direct dynamics in sterically hindered S_N2/E2 reaction. Chem Sci. 2018; 9 :693–701. [PubMed: 29629138]
31. Zhang J, Xie J, Hase WL. Dynamics of the $F^- + CH_3I \rightarrow HF + CH_2I^-$ proton transfer reaction. J Phys Chem A. 2015; 119 :12517–12525. [PubMed: 26473337]
32. Walden P. Über die gegenseitige Umwandlung optischer Antipode. Ber Dtsch Chem Ges. 1896; 29 :133–138.
33. Eppink ATJB, Parker DH. Velocity map imaging of ions and electrons using electrostatic lenses: Application in photoelectron and photofragment ion imaging of molecular oxyge. Rev Sci Instrum. 1997; 68 :3477–3484.
34. Wester R. Velocity map imaging of ion-molecule reaction. Phys Chem Chem Phys. 2014; 16 :396–405. [PubMed: 24195964]
35. Bastian B, et al. Imaging reaction dynamics of $F^-(H_2O)$ and $Cl^-(H_2O)$ with CH_3I. J Phys Chem A. 2020; 124 :1929–1939. [PubMed: 32050071]
36. Fateley WG, Miller FA. Torsional frequencies in the far infrared-III: The form of the potential curve for hindered internal rotation of a methyl grou. Spectrochim Acta. 1963; 19 :611–628.
37. Gyoôri T, Czakó G. Automating the development of high-dimensional reactive potential energy surfaces with the ROBOSURFER program system. J Chem Theory Comput. 2020; 16 :51–66. [PubMed: 31851508]
38. Xie Z, Bowman JM. Permutationally invariant polynomial basis for molecular energy surface fitting via monomial symmetrization. J Chem Theory Comput. 2010; 6 :26–34. [PubMed: 26614316]
39. Werner, H-J; , et al. MOLPRO, version 2015.1, a package of ab initio programs. See http://www.molpro.net
40. Hase, WL. Encyclopedia of Computational Chemistry. Vol. 1. Wiley; New York, NY: 1998. 399–402. chap

Europe PMC Funders Author Manuscripts

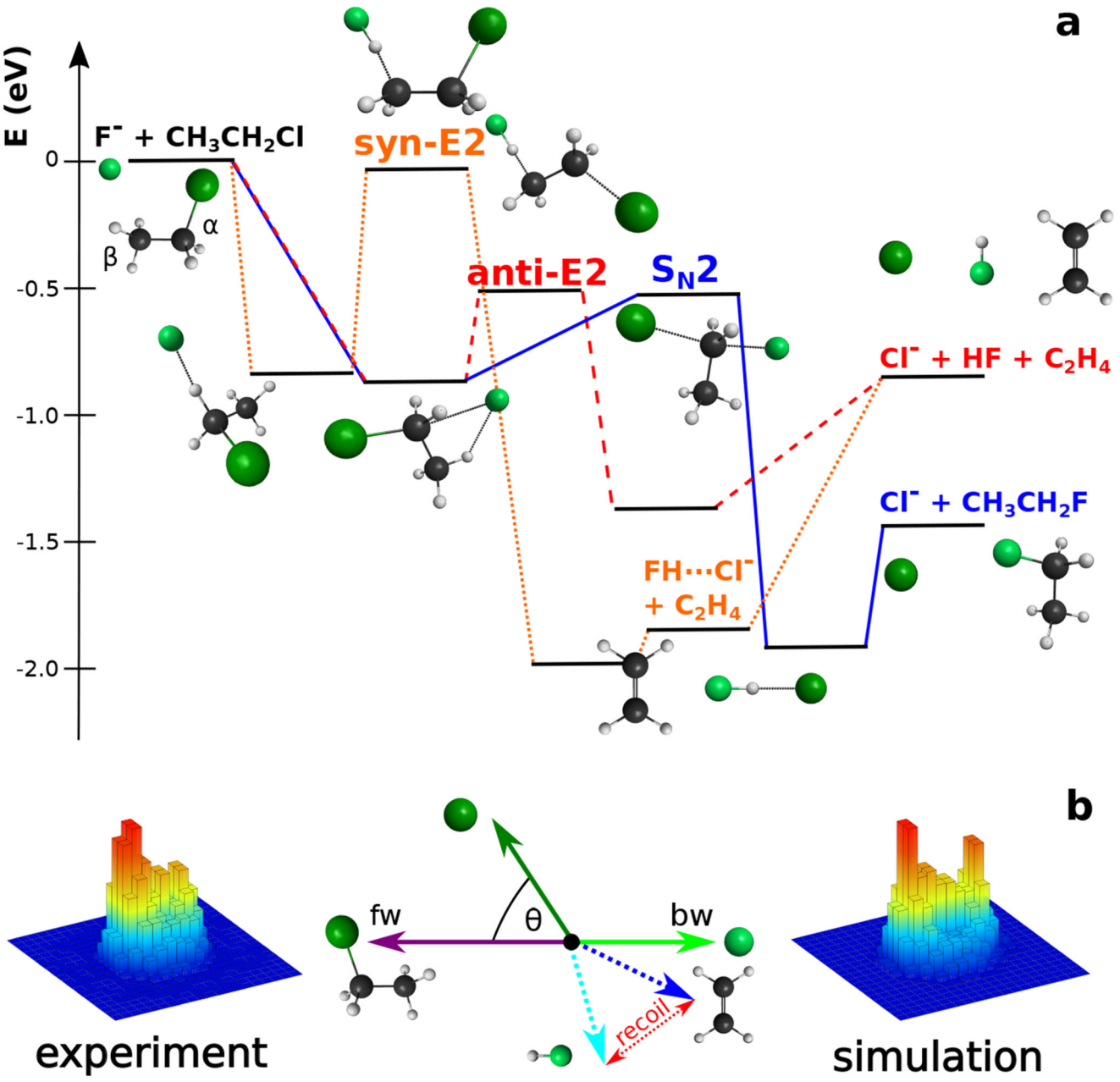

Figure 1. Reaction of $F^- + CH_3CH_2Cl$.

a Minimum energy pathway (MEP) illustrating the three most important reaction channels: anti-E2 (dashed red), syn-E2 (dotted orange), and S_N2 (solid blue). Structures show the atomic arrangement in the transition states (TS) and pre-reaction minima. For S_N 2, the classic Walden inversion TS is depicted[32]. Syn- and anti-E2 are termed after the relative orientation of the attacking base (F^-), the carboncarbon bond and the leaving group (Cl) in the transition state. The E2 TS requires a planar arrangement of the three involved bonds of CH_3CH_2Cl: the C_β-H bond, the C-C bond, and the C_α-Cl bond (MEP and structures adapted from [15,23]). b Velocity distributions of Cl^- product ions at 0.35 eV collision energy are shown from experiment and simulation together with a sketch of a Newton diagram

depicting the relative orientations of reactant and product beams. The dashed arrows indicate the velocities of the neutral products with the red arrow illustrating the recoil of HF and C_2H_4 from each other. Forward (fw) is defined along the original direction of the CH_3CH_2Cl beam.

Europe PMC Funders Author Manuscripts

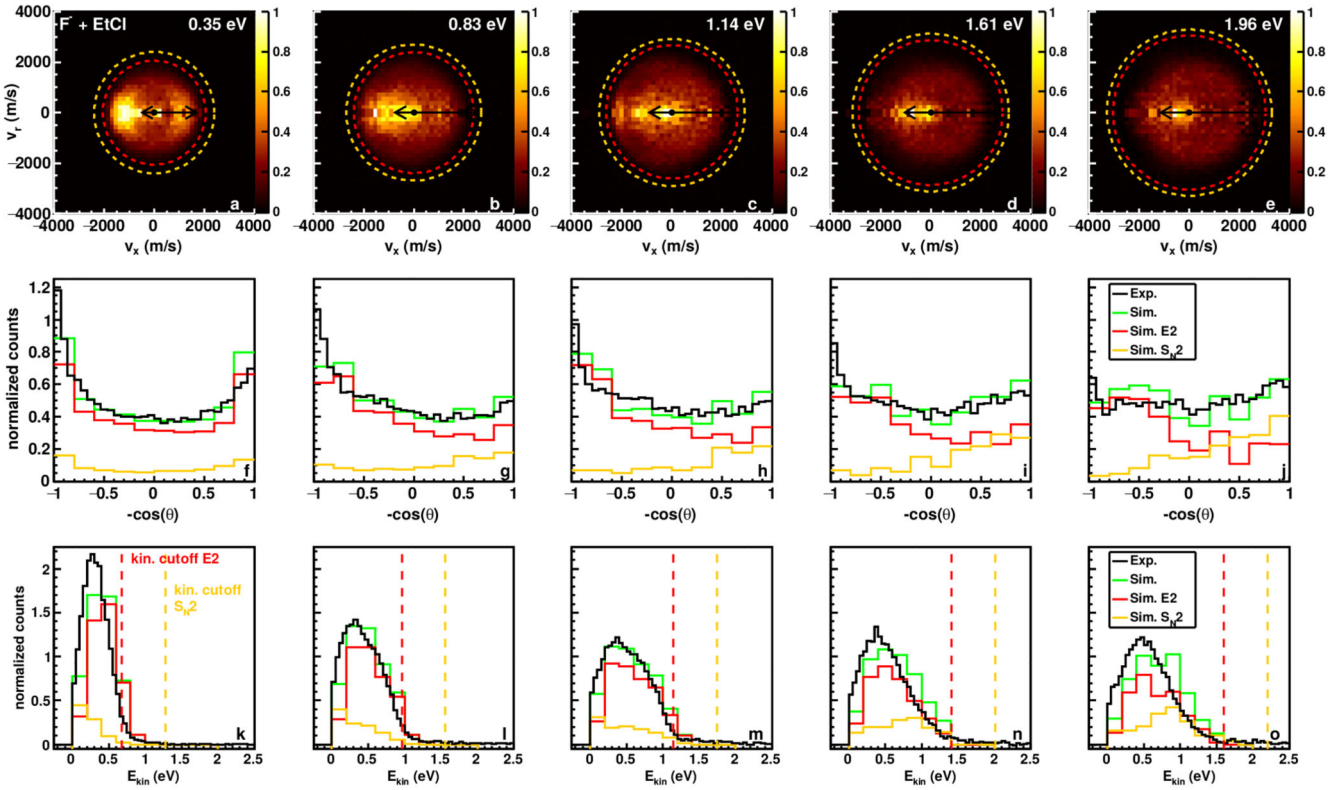

Figure 2. Differential scattering cross sections.

a–e Two-dimensional representation of the experimental 3D scattering distribution of $^{35}Cl^-$ product ions (0.35–1.96 eV). Superimposed circles represent the kinematic cutoff for S_N2 (orange) and E2 (red). The Newton diagram is given in Fig. 1b. Forward scattering is defined for a scattering angle θ = 0° – 90° and backward scattering for θ = 90° – 180° **f–j** Velocity integrated angular distributions and **k–o** product ion kinetic energy distributions Ekin. In the middle and bottom panel, the total distributions including all product channels forming Cl^-, are given for experiment and theory in black and green, respectively. Individual contributions from E2 (red, combined anti-E2 and syn-E2) and S_N2 (orange) are scaled according to their respective integral cross sections (Supplementary Table 3). Dashed lines in the bottom panel represent the kinematic cutoffs for E2 (red) and S_N2 (orange). Exp. data for Erel = 1.96 eV taken from [17].

Europe PMC Funders Author Manuscripts

Europe PMC Funders Author Manuscripts

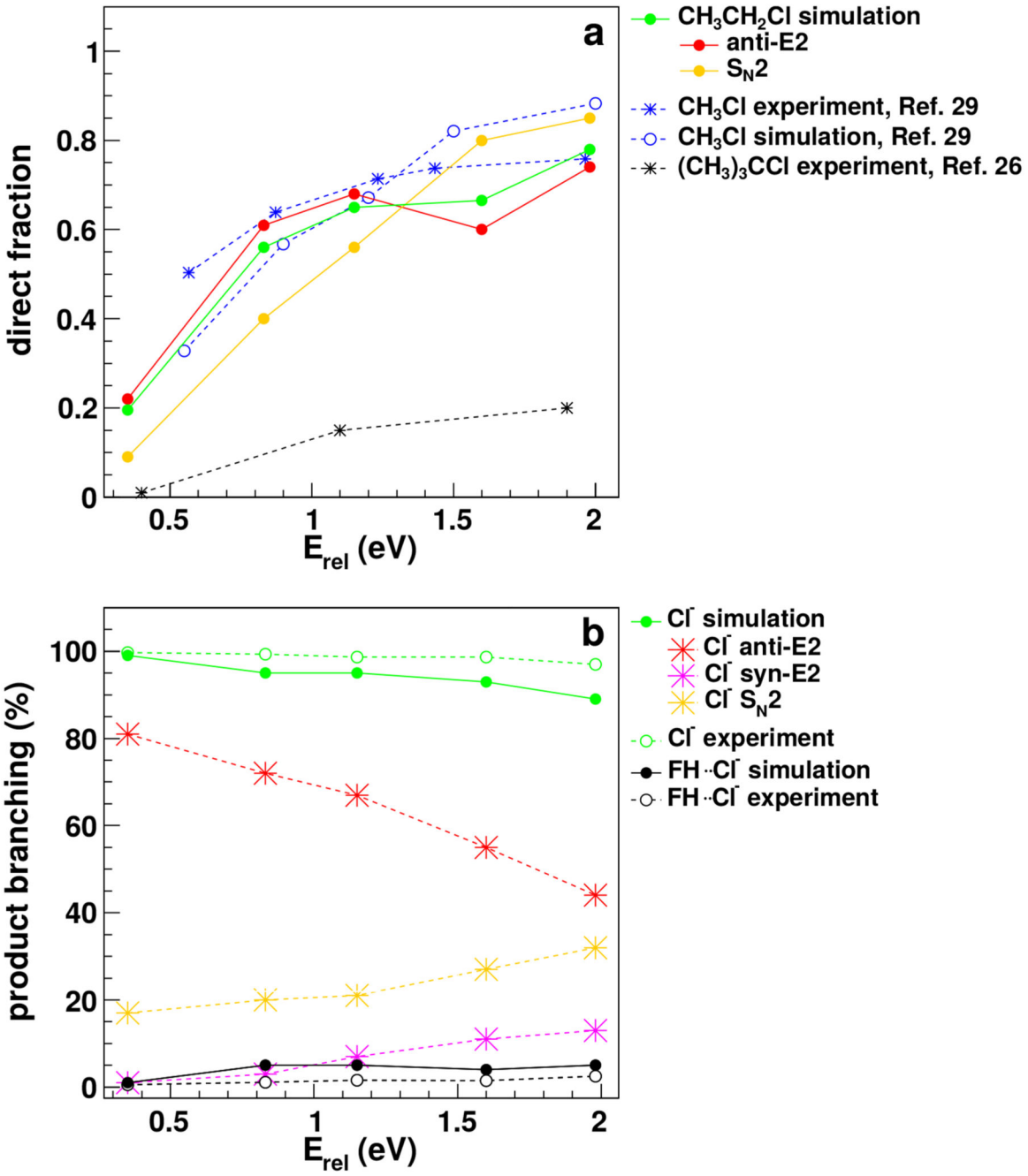

Figure 3. Direct fractions and product branching ratios.

a Fraction of direct trajectories for anti-E2 (red), S_N2 (orange), and their sum (green) as a function of relative collision energy. As comparison, direct fractions for $F^- + CH_3Cl$[28] (blue stars: exp., blue open circles: sim.) and $F^- + (CH_3)_3CCl$[25] (grey stars: exp.) are given. b Product branching for Cl^- (green) and FH...Cl^- ions (black) (exp.: open symbols, sim.: filled symbols). The contributions to Cl^- of anti-E2, syn-E2 and S_N2 are also displayed separately. FH...Cl^- stems solely from syn-E2. Contributions of CH_3CHCl^- product ions are not

displayed for clarity. Supplementary Table 1 gives the numerical values and their accuracies for all three product ions.

Europe PMC Funders Author Manuscripts

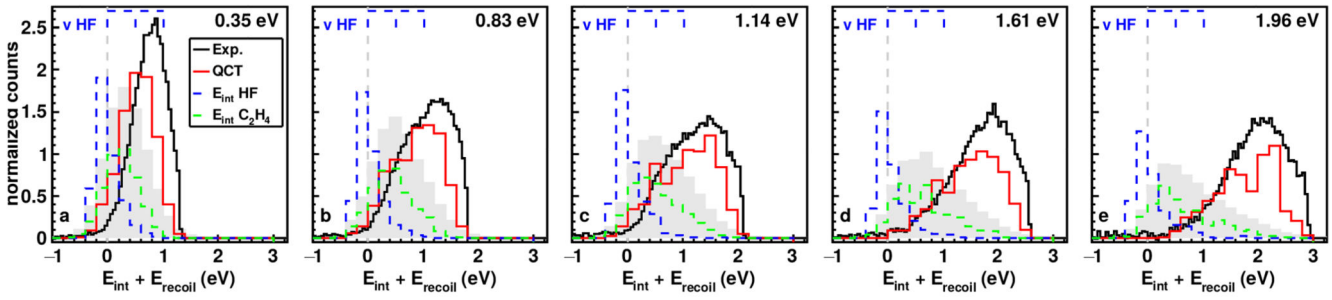

Figure 4. Internal energy E_{int} distributions for the E2 reaction.

(a–e). In addition to the internal energy of HF and CH_2CH_2 the experimental curve contains the relative recoil energy Erecoil between HF and CH_2CH_2 (exp: solid black, sim: solid red). Dashed curves show the individual internal energy distributions for HF (dashed blue) and CH_2CH_2 (dashed green) with the sum of both distributions given by the gray shaded area. The difference between the red and gray distributions indicates the energy channeled into recoil of both neutral products. The blue bars illustrate the vibrational quanta in the HF stretching mode. Distributions are area normalized and simulations weighted by the branching ratio of E2 vs S_N2 (blue/green normalized to 1; red/gray normalized to 2). Exp. data for Erel = 1.96 eV taken from [17].

Europe PMC Funders Author Manuscripts